Biologically Inspired Ultrathin Contact Imager for High-Resolution Imaging of Epidermal Ridges on Human Finger

Kyung-Won Jang, Kisoo Kim, Sang-In Bae, and Ki-Hun Jeong*

Compound eyes exhibit compelling vision schemes due to their unique visual ultrastructures. Here, a biologically inspired ultrathin contact imager (BUCI) for high-resolution contact fingerprint imaging is reported. The BUCI contains ultrathin arrayed camera, light-emitting diode arrays, and light guide plate (LGP). The ultrathin arrayed camera is fully packaged with microlens arrays, variable micropinhole arrays (MLA-VMA), and a single complementary metal oxide semiconductor image sensor. The ultrathin arrayed camera shows a large field of view of 77.3° and a constant MTF50 of 89.4 cycles mm^{-1}, relatively higher than a comparable single lens camera at the distance less than 36.8 mm. The channel images of a human fingertip are directly obtained by using frustrated total internal reflection and stitched to a single and high-resolution full-field image for a fingertip of 5.7 mm × 4.9 mm. The BUCI provides a new platform for high-resolution contact imaging in biometric or healthcare applications.

1. Introduction

Compound eyes contain hundreds and thousands of multiple apertures with tiny facet lenses for some intriguing visual functions such as large field of view (FOV), minimal off-axis aberration, and infinite depth of field (DOF).[1–4] In particular, the facet lenses facilitate short working-distance imaging and scale down the imaging system, thanks to their short focal length and small aperture size.[5] They also have high sensitivity to motion detection, whereas the spatial resolution is relatively low, compared with camera eyes.[6,7] Unlike other compound eyes, *Xenos peckii*, an endoparasite of paper wasp, exhibits distinct anatomical features, which consist of large aperture lenses, pigmented cups, and multiple photoreceptor cells.[8–10] As a result, this unique eye obtains high-resolution and short-distance imaging with a wide FOV.[11]

K.-W. Jang, K. Kim, S.-I. Bae, Prof. K.-H. Jeong
Department of Bio and Brain Engineering
Korea Advanced Institute of Science and Technology (KAIST)
291 Daehak-ro, Yuseong-gu, Daejeon 34141, Republic of Korea
E-mail: kjeong@kaist.ac.kr
K.-W. Jang, K. Kim, S.-I. Bae, Prof. K.-H. Jeong
KAIST Institute for Health Science and Technology
KAIST
Daejeon 34141, Republic of Korea

The ORCID identification number(s) for the author(s) of this article can be found under https://doi.org/10.1002/admt.202100090.

For a last decade, compound eye cameras have been actively reported depending on their configurations such as curved or planar types.[12–14] The curved configuration often exhibits microlens arrays (MLA) on hemispherical shapes using complicate fabrication methods such as integration with curved complementary metal oxide semiconductor (CMOS) image sensor arrays (ISA) or additional optical relay components to guide light to planar CMOS ISA.[15–20] The curved configuration can provide a large FOV but has low resolution and it is very difficult to manufacture at the wafer-level.[15,16] In contrast, the planar configuration facilitates the wafer-level fabrication as well as the compact camera packaging.[21–23] Recently, an ultrathin arrayed camera inspired from *X. peckii* vision principle has been demonstrated by employing inverted MLA without optical crosstalk.[24] The arrayed camera shows a set of partial images with slightly different views and allows high contrast and high-resolution imaging after the image reconstruction. However, the compound eye cameras have not yet been utilized for short-working-distance imaging applications.

Here, we report biologically inspired ultrathin contact imager (BUCI) for high-resolution contact imaging of epidermal ridges on a human finger. The BUCI consists of ultrathin arrayed camera, light-emitting diode (LED) arrays, and light guide plate (LGP). Inspiring the vision scheme of *X. peckii*, the ultrathin arrayed camera features inverted MLA with variable micropinhole arrays (VMAs) on a single CMOS image sensor (Sony IMX 219, 8 MP, unit pixel: 1.12 μm × 1.12 μm, frame rate: 30 fps) (**Figure 1**a). The VMAs emulate the optical function of the microtrichia and the pigmented cup of *X. peckii* eye. The unique structures efficiently block stray light from reaching the image sensor and thus remove the optical crosstalk between neighboring microlenses. The diameter of micropinhole on each layer determines the camera performance such as contrast, FOV, or image resolution. The inverse configuration of MLA substantially increases the FOV of a single microlens due to additional refraction from the top surface and effectively reduces the gap distance between the MLA and the image sensor (see Figure S1, Supporting Information). Light from LED arrays for contact imaging is guided into a LGP. Back scattered light on the contact surface between the ridge of finger and the LGP is captured onto the BUCI due to frustrated total internal reflection (FTIR) (Figure 1b). Each channel image from the MLA is reconstructed to a single and high-resolution full-field image of fingerprint after the image stitching process, which contains trimming,
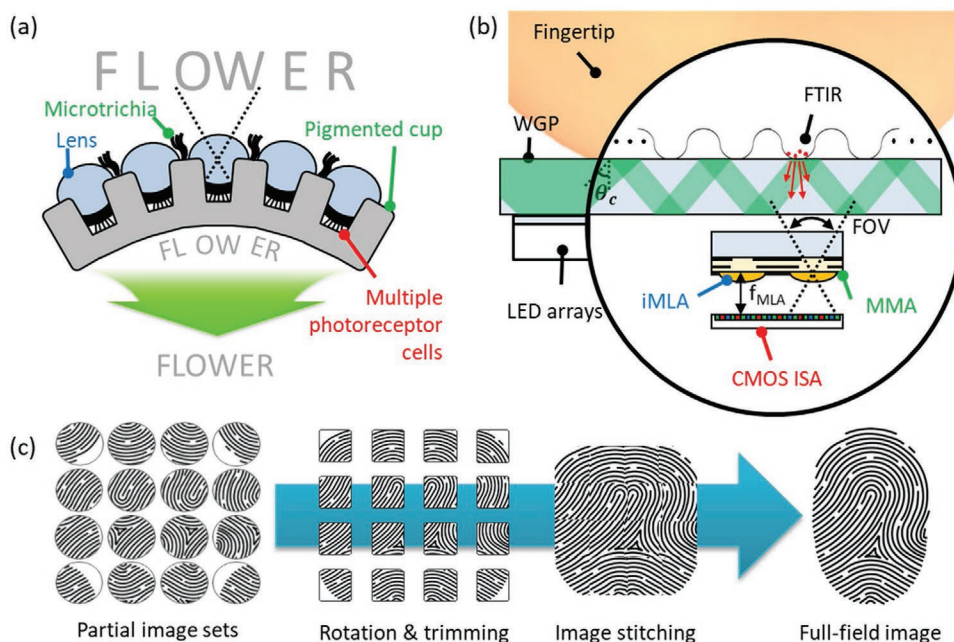
**ADVANCED
SCIENCE NEWS**
www.advancedsciencenews.com

**ADVANCED
MATERIALS
TECHNOLOGIES**
www.advmattechnol.de

Figure 1. Schematic diagram of BUCI. Working principles of a) *X. peckii* eye. b) BUCI consisting of ultrathin arrayed camera, LED arrays, and LGP. Light from LED arrays is guided into a LGP, where scattered light at the contact surface between the finger and the top surface is captured onto the BUCI due to FTIR. c) An image reconstruction process from multiple channel images to a full-field image. Each channel image is captured by a single microlens without optical crosstalk and stitched for high-resolution full-field imaging.

orientation correction, and stitching of multiple channel images (Figure 1c). The BUCI can provide high-resolution optical image of human fingertip for high level biometric security, visualizing the minutiae types such as core, ridge ending, and bifurcation.

2. Results and Discussion

2.1. Device Fabrication

The ultrathin arrayed camera is achieved by employing the microfabrication of MLA-VMA and the integration with a single CMOS image sensor (**Figure 2**a). First, a 10 µm thick black photoresist resin (GMC 1040, Gersteltec, Switzerland) and a 20 µm thick transparent photoresist resin (SU-8 2025, Micro-Chem Corp.) are repeatedly spin-coated and photolithographically defined on a 4 in. borosilicate glass wafer. Note that the multiple layers of black resin above 20 µm in thickness more efficiently absorb light in visible range, compared to a single layer of black resin (see Figure S2, Supporting Information) and thus they block the optical crosstalk between microlenses. The adhesion between transparent and black resins was substantially increased by using oxygen plasma treatment. A positive photoresist resin (AZ9260, MicroChem Corp.) was then defined to form MLA (lens diameter: 150 µm, f/1.6) after thermal reflow. The MLA-VMA was inversely integrated on a CMOS image sensor after wafer dicing by placing four 240 µm thick Al_2O_3 microposts with epoxy glue. The scanning electron microscopic (SEM) images show the MLA is optically aligned with the VMA (Figure 2b). The cross-sectional optical image confirms that the VMA consist of three micropinhole layers, which are separated with transparent SU-8 and well aligned along the optical axes of

MLA (Figure 2c). The captured image also shows the MLA-VMA has the physical dimension of 6.1 mm × 5.2 mm (Figure 2d). Note that the area of MLA-VMA is larger than the active pixel area of a CMOS image sensor to block stray light from the interstitial gap between the MLA-VMA and the image sensor. The optical images show the ultrathin arrayed camera (Figure 2e,f), where the side-view image of MLA-VMA confirms that the image sensor is precisely placed at the focal length of MLA.

2.2. MTF and FOV Measurement of Ultrathin Arrayed Camera

The MTF was measured for contact imaging through the ultrathin arrayed camera and compared with that of a commercial single-lens camera (Raspberry Pi camera V2, 8 MP, f/1.6) under a constant f-number for both microlenses and a single lens (**Figure 3**a). In this experiment, a slanted vertical edge image was first obtained by both cameras depending on the object distance, ranging from 10 to 110 mm. The image size of a single-lens camera was resized to the same size as each channel in the ultrathin arrayed camera and the edge sharpness of a slanted vertical edge image was then calculated for the comparison of MTF using a lens testing software (Quick MTF, Inc.). The experimental results clearly demonstrate that the ultrathin arrayed camera maintains a constant MTF50, even higher than the single-lens camera within a short distance. For instance, the MTF50 for the ultrathin arrayed camera shows 89.4 cycles mm^{-1}, i.e., three times higher than that for the single-lens camera at 10mm in object distance and still higher at less than 36.8 mm. As a result, the ultrathin arrayed camera is very suitable for high-resolution imaging within a short distance. The FOV of individual channels is mainly controlled by
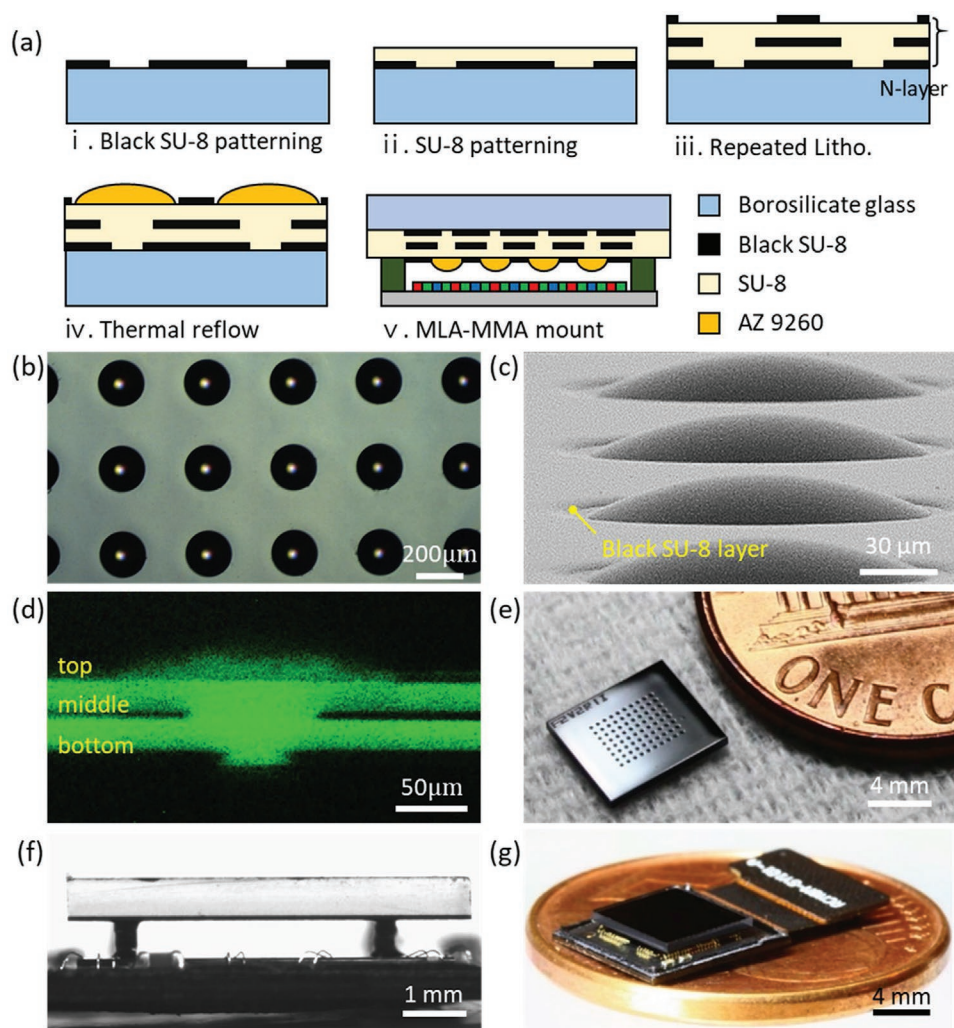
2100090 (2 of 7)

Figure 2. Microfabrication and configuration of the ultrathin camera. a) Microfabrication procedures for MLA-VMA, fabricated by using repeated photolithography and thermal reflow. b) Microscopic image and c) scanning electron micrographs of MLAs. d) Microscopic image of cross section at VMAs, centered well below MLAs. Optical images of e) MLA-VMA after dicing and f) MLA-MMA mounted on CMOS image sensor. g) Optical image of the ultrathin arrayed camera after integrating MLA-VMA on CMOS ISA.

the top micropinhole diameter of VMA (Figure 3b). The FOV is decided by using trigonometry of half width of image on a single image sensor and the image distance and also confirmed by ray tracing based on the height and radius of top micropinhole of VMA (see Figure S3, Supporting Information). Note that the FOV determines not only the total area of a single channel image on a CMOS image sensor but also the edge overlap region between channel images under a constant pitch of microlenses. Note that the MLA with a large FOV effectively increases the edge overlap region and thus allows blind-free image stitching without any additional design[25] (see Figure S4, Supporting Information). The FOV measurement was done by using trigonometry of the object distance and the full width of a single channel image, which contains 3.5 mm linear graduations. The top micropinhole diameter varies from 21 to 69 µm, corresponding to 50° to 77.3° for FOV. Note that the middle micropinhole diameter of VMA decreases FOV when it is smaller than the top micropinhole diameter of VMA (see

Figure S5, Supporting Information). The MTF was analyzed along the incident angle of light by changing the middle micropinhole diameter of VMA because the image stitching requires high MTF in edge overlap region (Figure 3c). Light at normal incidence reaches the center of image area, whereas light at the maximum incident angle enters the edge of image area. Therefore, the MTF in the edge region increases with the intensity of light at the maximum incident angle. The MTF50 was measured by using the slanted vertical edge image, rotating every 5° from 0° to 15°. The middle micropinhole diameter also varies from 21 to 69 µm at a constant top micropinhole diameter of 44 µm and every MTF50 at each incident angle increases, corresponding to the middle micropinhole diameter (MTF50 at 0° increases from 144.3 to 164.5 cycles mm^{-1} and MTF50 at 15° increases from 78.2 to 116.6 cycles mm^{-1}). In particular, the increment of MTF50 becomes large at a large incident angle, which increases the image resolution at the edge of image (MTF50 is increased from 20.2 cycles mm^{-1}
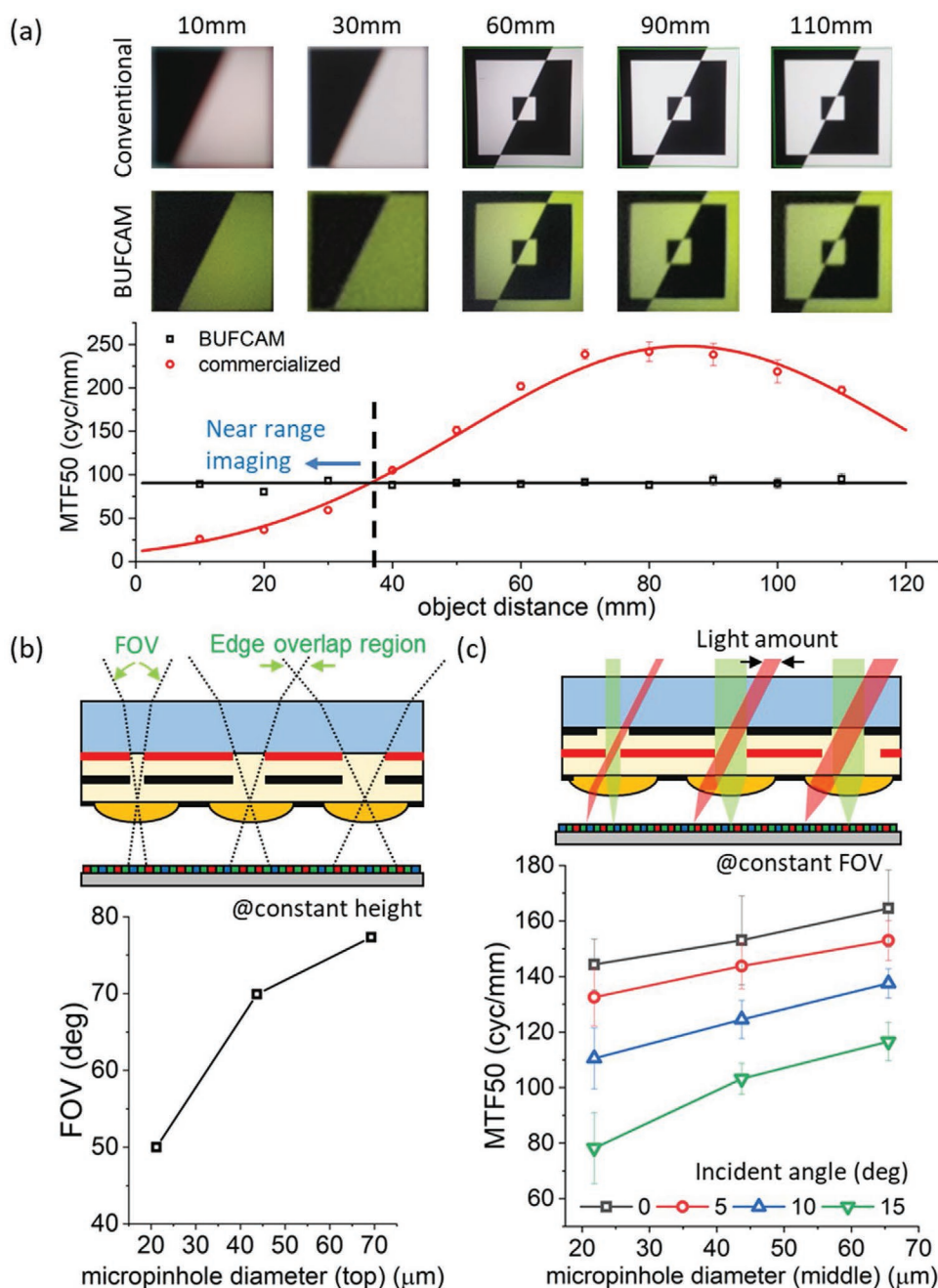
Figure 3. MTF and FOV measurement. a) Measured MTF50 depending on an object distance. Unlike conventional camera, the ultrathin arrayed camera exhibits a constant MTF50 along the overall object distance and even higher MTF50 at the distance less than 36.8 mm. All the MTFs were calculated from the fine edge sharpness in captured slanted images. b) FOV measurement of top layer in VMA. The FOV is controlled by adjusting the diameter of top micropinhole. c) MTF50 depending on the diameter of the middle micropinhole under a constant FOV. The aperture diameter is mainly controlled by the diameter of middle micropinhole, which adjusts the image resolution as well as the amount of light.

at $0°$–38.4 cycles mm^{-1} at $15°$). As a result, the VMA should have wider micropinhole diameter of lower layer than that of upper layer to improve the MTF at the edge. In experiment, the ultrathin camera captured the USAF 1951 resolution chart under backlight illumination. The resolvable line pair is the element 5 of group 5, which corresponds to resolvable line width of 9.84 µm (see Figure S6, Supporting Information).

2.3. Frustrated TIR-Based Contact Fingerprint Imaging

The BUCI was fully packaged with LED arrays for high-resolution FTIR imaging by using a 4 mm thick aluminum zig (**Figure 4**a). LED arrays (LXZ1-PM01, peak wavelength at 530 nm) are mounted on the LGP using UV resin (NOA 63) as an index matching material and LED light is then guided
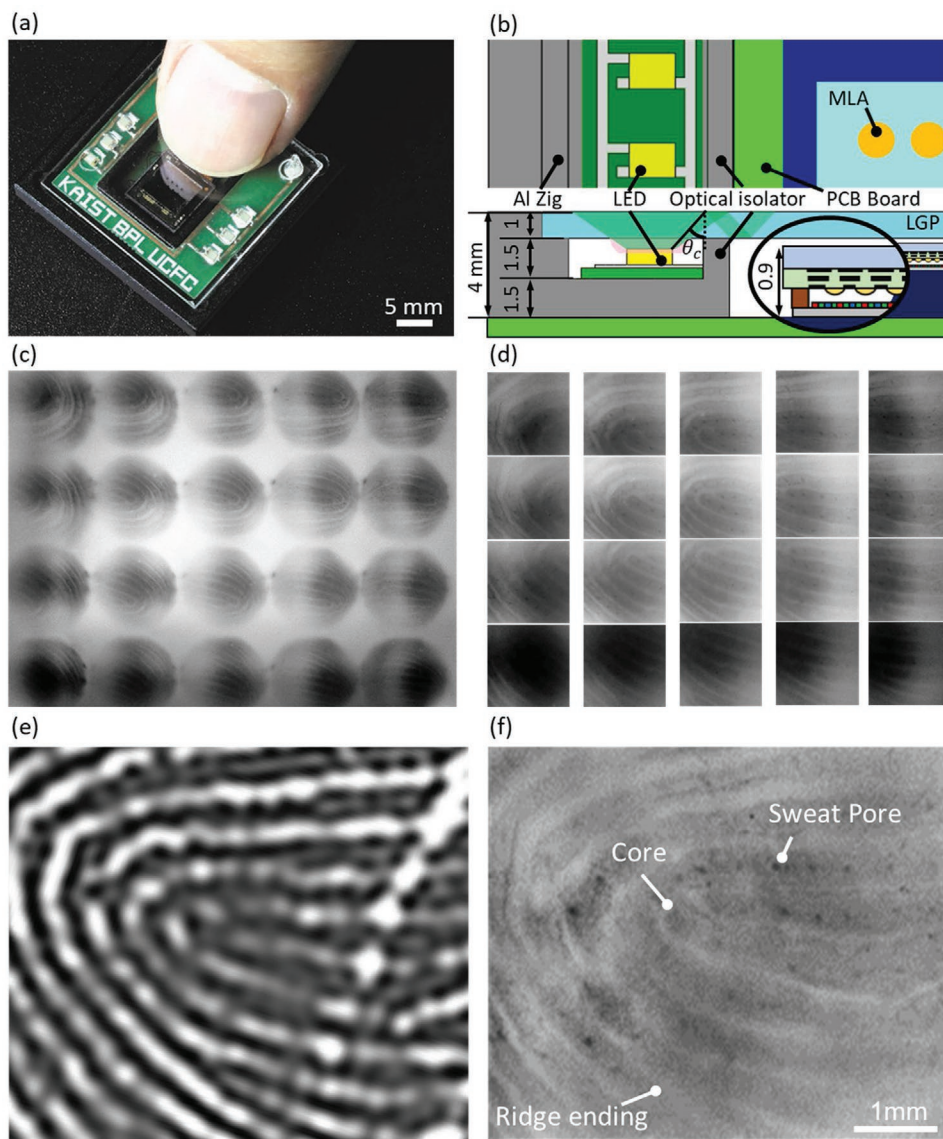
Figure 4. Captured fingerprint images through the BUCI. a) Optical image of fully packaged BUCI with LED units. b) Physical dimension of the BUCI in packaging scheme. The optical isolator of Al zig is used for blocking the directly entered light from LED units to CMOS ISA. c) Captured image of real fingerprint through the BUCI. d) Image extraction by image trimming and rotation. e) Fingerprint image obtained by commercialized capacitive fingerprint sensor. f) A full-field image stitched from channel images, corresponding to an area of 5.7 mm × 4.9 mm of human fingertip.

into the LGP at an incident angle that exceeds the critical angle between glass and air (Figure 4b). The aluminum zig blocks ambient light that may decrease the image contrast. The fully packaged BUCI captures the array images of epidermal ridges on a human finger on the LGP from scattered light at the surface between the fingertip and LGP (Figure 4c). The channel images of each microlens visualizes fingerprint without any optical crosstalk. All the channel images were rotated and trimmed for image stitching (Figure 4d). For comparison, the fingerprint image was also obtained by using conventional capacitive fingerprint sensor (FPC1020, Fingerprint Card AB, 192 × 192 pixels, 508 dpi) (Figure 4e). The full-field image was finally reconstructed after image stitching with all the channel images (Figure 4f). The reconstructed image not only visualizes

a large area of 5.7 mm × 4.9 mm for human fingertip (2.1 times wider than the width of extracted channel image with 2.7 mm) but also clearly distinguishes sub-features of human fingertip such as core, ridge ending, and even sweat pores unlike conventional capacitive sensors.

3. Conclusion

In summary, we have successfully demonstrated high-resolution contact fingerprint imaging by utilizing the ultrathin arrayed camera and FTIR illumination. The BUCI features the fully integrated imaging system of 4 mm in total thickness, containing MLA-VMA, LGP with LED arrays, and a single CMOS

image sensor. The BUCI shows FOV of 77.3° and relatively high MTF of 89.4 cycles mm⁻¹. The fully reconstructed fingerprint image demonstrates clear sub-features of human finger such as core, ridge ending, and even sweat pores. The BUCI can provide a new platform for not only high level of biometric security in mobile applications but also high-resolution contact imaging in diverse wearable or healthcare applications.

4. Experimental Section

Experiment Setup and Method of FOV and MTF Measurement: The BUCI captured a ruler with period of 3.5 mm on an OLED panel, located 25 mm away. The FOV was calculated by using triangulation for the object distance and the width of ruler. The edge of image was clearly decided by using the FWHM of image intensity. In addition, the BUCI captured a slanted image of an OLED display panel target mounted on the rail. The captured images become smaller as the OLED display moves from 10 to 120 mm. The sizes of both images from conventional camera and the BUCI were fit to each other, depending on the object distance for precise comparison of MTF. Next, the BUCI also captured slanted images by rotating the OLED display from 0° to 15°. Both the cameras captured five images at every 5° and their MTFs were calculated four times at each image.

Image Reconstruction Algorithms: The image reconstruction algorithm consists of two main parts: alignment and compositing.[26,27] First, each channel image was extracted and trimmed as a square size for image stitching without distortion. Other channel images were then aligned with a center channel image by using local feature matching with a DAISY descriptor.[28] The fingerprint features were composited by using an interactive, computer-assisted framework because all the channel images have barrel distortion in edge by high NA lens. All the features were seamlessly combined by the graph-cut optimization. Additional remaining visible artefacts in the composite were also reduced by the gradient-domain fusion, based on the Poisson equation. The reconstructed fingerprint image was finally achieved by using these reconstruction algorithms.

Supporting Information

Supporting Information is available from the Wiley Online Library or from the author.

Acknowledgements

Conflict of Interest

The authors declare no conflict of interest.

Author Contributions

K.-W.J. and K.-H.J. conceived the idea and wrote the manuscript. K.-W.J., K.K., and S.-I.B. performed the experiments and analyzed the data. K.-H.J. supervised this research.

Data Availability Statement

The data that support the findings of this study are available from the corresponding author upon reasonable request.

Keywords

[1] D. G. Stavenga, R. C. Hardie, *Facets of Vision*, Springer, Berlin **2012**.
[2] M. F. Land, D. E. Nilsson, *Animal Eyes*, Oxford University Press, Oxford **2012**.
[3] E. Warrant, D. E. Nilsson, *Invertebrate Vision*, Cambridge University Press, Cambridge **2006**.
[4] M. F. Land, *Contemp. Phys.* **1988**, *29*, 435.
[5] A. J. Ijspeert, T. Masuzawa, S. Kusumoto, *Biologically Inspired Approaches to Advanced Information Technology*, Springer **2006**.
[6] V. Lakshminarayanan, M. K. Parthasarathy, *J. Mod. Opt.* **2016**, 1.
[7] K. Kirschfeld, in *Neural Principles in Vision. Proceedings in Life Sciences* (Eds: F. Zettler, R. Weiler), Springer, Berlin **1976**, pp. 354–370.
[8] E. Buschbeck, B. Ehmer, R. Hoy, *Science* **1999**, *286*, 1178.
[9] E. K. Buschbeck, B. Ehmer, R. R. Hoy, *J. Comp. Physiol., A* **2003**, *189*, 617.
[10] S. Maksimovic, J. E. Layne, E. K. Buschbeck, *J. Exp. Biol.* **2007**, *210*, 2819.
[11] D. Keum, K. W. Jang, D. S. Jeon, C. S. Hwang, E. K. Buschbeck, M. H. Kim, K. H. Jeong, *Light: Sci. Appl.* **2018**, *7*, 1.
[12] T. Chung, Y. Lee, S. P. Yang, K. Kim, B. H. Kang, K. H. Jeong, *Adv. Funct. Mater.* **2018**, *28*, 1705912.
[13] Y. Cheng, J. Cao, Y. Zhang, Q. Hao, *Bioinspiration Biomimetics* **2019**, *14*, 031002.
[14] S. Wu, T. Jiang, G. Zhang, B. Schoenemann, F. Neri, M. Zhu, C. Bu, J. Han, K. D. Kuhnert, *Artif. Intell. Rev.* **2017**, *48*, 573.
[15] D. Floreano, R. Pericet-Camara, S. Viollet, F. Ruffier, A. Brückner, R. Leitel, W. Buss, M. Menouni, F. Expert, R. Juston, M. K. Dobrzynski, G. L'Eplattenier, F. Recktenwald, H. A. Mallot, N. Franceschini, *Proc. Natl. Acad. Sci. USA* **2013**, *110*, 9267.
[16] Y. M. Song, Y. Xie, V. Malyarchuk, J. Xiao, I. Jung, K. J. Choi, Z. Liu, H. Park, C. Lu, R. H. Kim, R. Li, K. B. Crozier, Y. Huang, J. A. Rogers, *Nature* **2013**, *497*, 95.
[17] W. L. Liang, J. G. Pan, G. D. J. Su, *Optica* **2019**, *6*, 326.
[18] H. Zhang, L. Li, D. L. McCray, S. Scheiding, N. J. Naples, A. Gebhardt, S. Risse, R. Eberhardt, A. Tünnermann, A. Y. Yi, *Opt. Express* **2013**, *21*, 22232.
[19] W. L. Liang, H. K. Shen, G. D. J. Su, *Appl. Opt.* **2014**, *53*, 3696.
[20] C. Shi, Y. Wang, C. Liu, T. Wang, H. Zhang, W. Liao, Z. Xu, W. Yu, *Opt. Express* **2017**, *25*, 32333.
[21] A. Brückner, J. Duparré, R. Leitel, P. Dannberg, A. Bräuer, A. Tünnermann, *Opt. Express* **2010**, *18*, 24379.
[22] J. Duparré, F. Wippermann, P. Dannberg, A. Bräuer, *Bioinspiration Biomimetics* **2008**, *3*, 046008.
[23] J. Tanida, T. Kumagai, K. Yamada, S. Miyatake, K. Ishida, T. Morimoto, N. Kondou, D. Miyazaki, Y. Ichioka, *J. Appl. Opt.* **2001**, *40*, 1806.

[24] K. Kim, K. W. Jang, J. K. Ryu, K. H. Jeong, *Light: Sci. Appl.* **2020**, *9*, 28.

[25] B. Xu, H. Li, S. Gao, X. Hua, C. Yang, C. Chen, F. Yan, S. Zhu, T. Li, *Adv. Photonics* **2020**, *2*, 066004.

[26] S. Winder, G. Hua, M. Brown, in *2009 IEEE Conf. on Computer Vision and Pattern Recognition*, IEEE, Piscataway, NJ **2009**, pp. 178–185.

[27] A. Agarwala, M. Dontcheva, M. Agrawala, S. Drucker, A. Colburn, B. Curless, D. Salesin, M. Cohen, *ACM Trans. Graphics* **2004**, *23*, 294.

[28] E. Tola, V. Lepetit, P. Fua, in *2008 IEEE Conf. on Computer Vision and Pattern Recognition*, IEEE, Piscataway, NJ **2008**, pp. 1–8.

2100090 (7 of 7)